

Random Close Packing of Disks and Spheres in Confined Geometries

Kenneth W. Desmond and Eric R. Weeks

Department of Physics, Emory University, Atlanta GA 30322

(Dated: February 12, 2022)

Studies of random close packing of spheres have advanced our knowledge about the structure of systems such as liquids, glasses, emulsions, granular media, and amorphous solids. When these systems are confined their structural properties change. To understand these changes we study random close packing in finite-sized confined systems, in both two and three dimensions. Each packing consists of a 50-50 binary mixture with particle size ratio 1.4. The presence of confining walls significantly lowers the overall maximum area fraction (or volume fraction in three dimensions). A simple model is presented which quantifies the reduction in packing due to wall-induced structure. This wall-induced structure decays rapidly away from the wall, with characteristic length scales comparable to the small particle diameter.

I. INTRODUCTION

In 1611 Kepler conjectured that the most efficient packing of spheres is the face center cubic packing (*fcc*), with packing fraction $\phi_{fcc} = \pi/\sqrt{18}$ [1]. In 1831, Gauss provided a partial proof to this conjecture, and more recently Hales presented a more complete proof [2] that is still being validated [1]. However, the *fcc* packing is highly ordered, and in many cases random packings are of interest, as they are easy to create. For example, a large range of packing fractions have been found for granular particles with a minimum mechanically stable volume fraction $\phi_{rlp} \approx 0.55$ [3, 4, 5], termed random loose packing. The maximum volume fraction for a randomly packed 3D system is $\phi_{rcp} \approx 0.64$, termed random close packing (*rcp*) [3, 4, 6, 7, 8].

The earliest known experimental study on the density of *rcp* was performed by Bernal and Mason [6]. In their experiment they repeatedly shook and compressed a rubber balloon full of spheres for sufficiently long enough time to reach a very dense state at $\phi_{rcp} = 0.637$. This result is sensitive to the preparation method, although the final volume fractions found are always close to 0.64 [9]. Computational studies are especially sensitive to protocol, with ϕ_{rcp} ranging between 0.64 and 0.68 [10, 11]. A broader range of mechanically stable packing fractions can be obtained by consider packings consisting of a polydisperse mixture of spheres or packings with non-spherical particles [12, 13, 14, 15, 16, 17, 18, 19, 20]. Some theoretical progress explaining random close packing has occurred [21, 22, 23, 24], although this is far from complete [1]. All of these studies are relevant to a wide range of problems including the structure of living cells [9], liquids [6], granular media [21, 22], emulsions [25], glasses [26], and amorphous solids [27].

While all of the above studies focus on infinite systems, real systems have boundaries and often these boundaries are important. Furthermore, in many cases samples are confined between closely spaced boundaries, with the confining size being only a few characteristic particle sizes across [28]. For example, when a liquid is confined its structure is dramatically changed with particles

forming layers near the wall, which ultimately affects the properties of the liquid [29, 30, 31, 32, 33, 34]. The shearing of confined dense colloidal suspensions shows the emergence of new structures not seen before [35]. The flow of granular media through hoppers [36, 37] or suspensions through constricted micro- and nanofluidic devices [38, 39, 40, 41] can jam and clog, costing time and money. Some studies examined the packing of granular particles in narrow silos, focusing on stresses between particles and the walls [42, 43, 44, 45]. Other studies noted that the particle packing in silos is layered near the walls [46, 47]. However, the influence of boundaries on ϕ_{rcp} has not been studied previously.

We present computer simulated *rcp* packings in confined geometries. In particular, we study binary mixtures to prevent wall-induced crystallization [48, 49, 50]. We create two-dimensional (2D) and three-dimensional (3D) packings between two parallel walls, with periodic boundary conditions in the other directions. Confinement significantly modifies the *rcp* states, with lowered values for ϕ_{rcp} reflecting an inefficient packing near the walls. This inefficient packing persists several particle diameters away from the wall, although its dominant effects are only within 1-2 diameters.

These results will be useful for understanding many other confined systems. For example, many experiments study how confinement modifies the glass transition; samples which have a well-characterized glass transition in large samples show markedly different properties when confined to small samples [28, 50, 51, 52, 53, 54, 55, 56, 57]. However, it's not clear if these changes are due to boundaries or finite size effects [58]. Our results show that boundaries significantly modify the packing, which may in turn modify behavior of these confined molecular systems [28].

The manuscript is organized as follows. Section II outlines the algorithm we use to generate confined *rcp* states. Section III shows how the total packing fraction, particle number density, and local order of confined *rcp* states change with confining thickness and distance from the confining boundary. Finally, Sec. IV provides a simple model that predicts the packing fraction dependence with confinement.

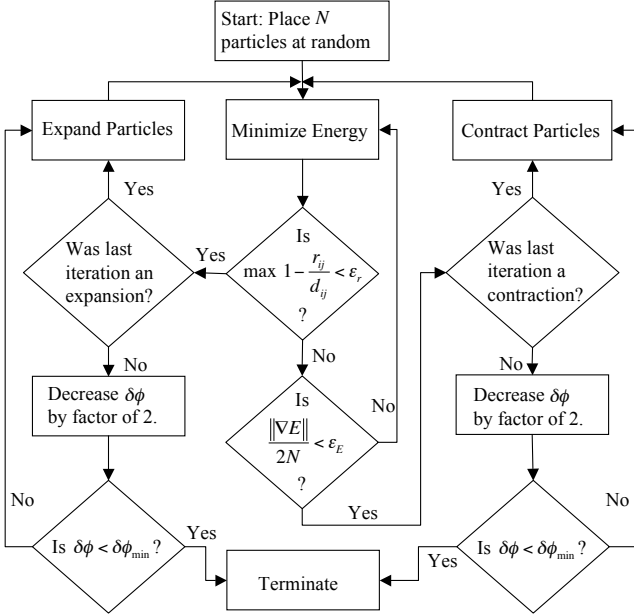


FIG. 1: A flow chart outlining our algorithm for computing *rcp* configurations.

II. METHOD

Our aim is to quantify how a confining boundary alters the structure of randomly closed packed (*rcp*) disks in 2D and spheres in 3D, and in particular to study how this depends on the narrowest dimension. This section presents our algorithm for 2D packings first, and then briefly discusses differences for the 3D algorithm.

In 2D, our system consists of a binary mixture of disks containing an equal number $N/2$ large disks of diameter d_l and small disks of diameter d_s with size ratio $\sigma = d_l/d_s = 1.4$. For each configuration, disks are packed into a box of dimensions L_x by L_y , with a periodic boundary along the x -direction and a fixed hard boundary (a wall) along the y -direction.

Each configuration is generated using a method adapted from Xu et al. [8] which is an extension of a method proposed by Clarke and Wiley [59]. This method is briefly summarized in Fig. 1. Infinitesimal particles are placed in the system, gradually expanded and moved at each step to prevent particles from overlapping. When a final state is found such that particles can no longer be expanded without necessitating overlap, the algorithm terminates. Near the conclusion of the algorithm, we alternate between expansion and contraction steps to accurately determine the *rcp* state.

In particular, while the final state found is consistent with hard particles (no overlaps allowed), the algorithm uses a soft potential at intermediate steps [8], given by

$$V(r_{ij}) = \frac{\epsilon}{2} (1 - r_{ij}/d_{ij})^2 \Theta(1 - r_{ij}/d_{ij}), \quad (1)$$

where r_{ij} is the center to center distance between two

disk i and j , ϵ is a characteristic energy scale ($\epsilon = 1$ for our simulations), $d_{ij} = (d_i + d_j)/2$, and $\Theta(1 - r_{ij}/d_{ij})$ is the Heaviside function making V nonzero for $r_{ij} < d_{ij}$. Simulations begin by randomly placing disks within a box of desired dimensions and boundary conditions with the initial diameters chosen such that $\phi_{\text{initial}} \ll \phi_{\text{rcp}}$. In the initial state particles do not overlap and the total energy $E = 0$.

Next all disk diameters are slowly expanded subject to the fixed size ratio $\sigma = 1.4$ and ϕ changing by $\delta\phi$ per iteration; we start with $\delta\phi = 10^{-3}$. After each expansion step, we check if any disks overlap, by checking the condition $1 - r_{ij}/d_{ij} > \epsilon_r = 10^{-5}$ for each particle pair. Below this limit, we assume the overlap is negligible. If any particles do overlap ($E > 0$), we use the non-linear conjugate gradient method [60] to decrease the total energy by adjusting the position of disks so they no longer overlap ($E = 0$). In practice, one energy minimization step does not guarantee we have reached a minimum within the desired numerical precision. Thus this step can be repeated to further reduce the energy if $E > 0$. We judge that we have reached a nonzero local minimum if the condition $\|\nabla E\|/(2N) < \epsilon_E = 10^{-7}$ is found, where $\|\nabla E\|$ is the magnitude of the gradient of E . Physically speaking this is the average force per particle, and the threshold value (10^{-7}) leads to consistent results.

If we have such a state with $E > 0$, this is not an *rcp* state as particles overlap. Thus we switch and now slowly contract the particles until we find a state where particles again no longer overlap (within the allowed tolerance). At that point, we once again begin expansion. Each time we switch between expansion and contraction, we decrease $\delta\phi$ by a factor of 2. Thus, these alternating cycles allow us to find an *rcp* state of non-overlapping particles (within the specified tolerance) and determine ϕ_{rcp} to high accuracy. We terminate our algorithm when $\delta\phi < \delta\phi_{\text{min}} = 10^{-6}$. In practice, we have tested a variety of values for the thresholds ϵ_r , ϵ_E , and $\delta\phi_{\text{min}}$ and find that our values guarantee reproducible results as well as reasonably fast computations. Our algorithm gave an average packing fraction of $\phi_{\text{rcp}} = 0.8420 \pm 0.0005$ for 40 simulated *rcp* states containing 10,000 particles with periodic boundary conditions along both directions. Our value of ϕ_{rcp} is in agreement with that found by Xu et al. [8].

The above procedure is essentially the same as Ref. [8]; we modify this to include the influence of the boundaries. To add in the wall, we create image particles reflected about the position of the wall; thus particles interact with the wall using the same potential, Eqn. 1.

Additionally, we wish to generate packings with pre-specified values for the final confining height $h = L_y/d_s$. (This allows us to create multiple *rcp* configurations with the same h .) We impose h by affinely scaling the system after each step, so that the upper boundary is adjusted by $L_y = h d_s$ and each disk's y -coordinate is multiplied by the ratio $L_{y,i+1}/L_{y,i}$, where $L_{y,i}$ and $L_{y,i+1}$ are the confining widths between two consecutive iterations. Thus

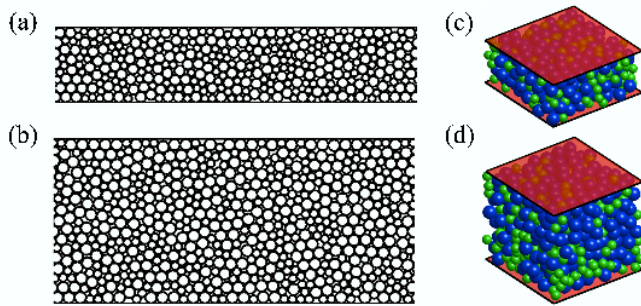


FIG. 2: (Color online). Illustrations of 2D and 3D configurations generated using the algorithm described in Sec. II. (a) 2D configuration for $h = 10$. (b) 2D configuration with $h = 20$. (c) 3D configuration with $h = 5$ where blue (dark gray) represents big particles and green (light gray) represents small particles. (d) 3D configuration with $h = 10$.

while d_s gradually increases over the course of the simulation, L_y increases proportionally so that the nondimensional ratio h is specified and constant. Some examples of our final *rcp* states are shown in Fig. 2.

To ensure we will have no finite size effects in the periodic direction, we examined ϕ_{rcp} for different h and L_x , and found $\phi_{rcp}(h)$ to be independent of L_x for $3 \leq h \leq 30$ if $L_x/d_s > 40$. Thus we have chosen N for each simulation to guarantee $L_x/d_s \approx 50$.

In 3D, our system consists of a binary mixture of spheres containing an equal number $N/2$ large spheres of diameter d_l and small spheres of diameter d_s with a size ratio $\sigma = d_l/d_s = 1.4$. Spheres are packed into a box of dimensions L_x by L_y by L_z , with periodic boundaries along the x - and z -directions and a fixed hard boundary along the y -direction. Each configuration is generated using the same particle expansion and contraction method described above and the same initial values for $\delta\phi$ and the terminating conditions. For each configuration $L_x = L_z$, $h = L_y/d_s$, and N is chosen so that $L_x/d_s > 10$. Our choice of $L_x/d_s > 10$ is not large enough to avoid finite effects. However, in order to acquire the large amount of data needed in a reasonable amount of time we intentionally choose a value of L_x/d_s below the finite size threshold. Trends observed in the 2D analysis will be used to support that any similar trends seen in 3D are real and not the result of the finite periodic dimensions. Note that in 3D we will show cases where $h > L_x/d_s$ resulting in the confining direction being larger than the periodic direction, and this may affect the structure of final configurations; however, we will not draw significant conclusions from those data.

Overall, it is not known if this algorithm produces mathematically rigorously defined random close packed states [8, 9, 61, 62]. However, the goal of this article is to determine empirically the properties of close-packed states in confinement, and we are not attempting to extract mathematically rigorous results. For example, we are not as interested in the specific numerical values of

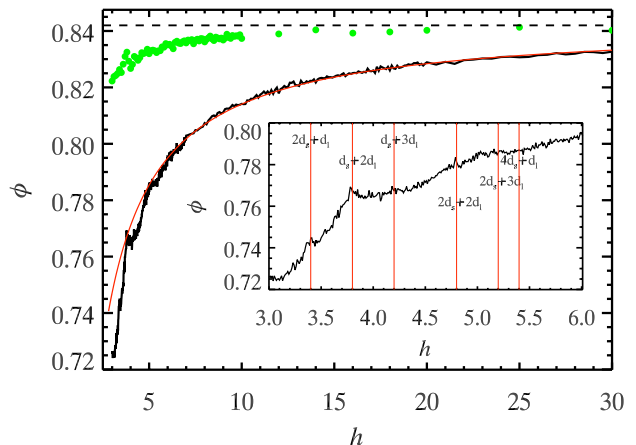


FIG. 3: (Color online). The black curve is the average packing fraction ϕ found by averaging at least 10 2D configurations together for various confining widths h ; recall that h has been nondimensionalized by d_s , the small particle diameter. The red curve (dark gray) is a fit using Eqn. 5 which finds $\phi_{rcp} = 0.842$ in the limit $h \rightarrow \infty$; the value for ϕ_{rcp} is indicated by the black dashed line. The green (light gray) data points are $\phi(h)$ computed for many configurations with the confining wall replaced by a periodic boundary. The inset is a magnified view of the region for $h \leq 6$ to better show the large variations within this range. The vertical lines in the inset are located at “special” h values where peaks and plateaus appear.

ϕ_{rcp} that we obtain, but rather the qualitative dependence on h . As noted in the introduction, different computational and experimental methods for creating *rcp* systems have different outcomes, and so it is our qualitative results we expect will have the most relevance.

Note that for the remainder of this paper, we will drop the subscript *rcp*, and it should be understood that discussions of ϕ refer to the final state found in each simulation run, $\phi_{rcp}(h)$.

III. RESULTS

A. 2D Systems

We begin by generating many 2D configurations with h between 3 - 30 and computing the packing fraction for each, as shown by the black curve in Fig. 3. This plot shows that confinement lowers ϕ , with the influence of the walls being increasingly important at lower h . The lowering of ϕ with confinement is most likely due structural changes in the packing near the confining boundary. We know that any alteration in particle structure from a *rcp* state must be “near” the wall because as $h \rightarrow \infty$ we expect to recover a packing fraction of ϕ_{rcp} , implying that in the infinite system the “middle” of the sample is composed of an *rcp* region. Extrapolating the data in Fig. 3 to $h \rightarrow \infty$ we find $\phi_{h \rightarrow \infty} = \phi_{rcp} = 0.842$ which is essentially a test of our method. The extrapolation (red

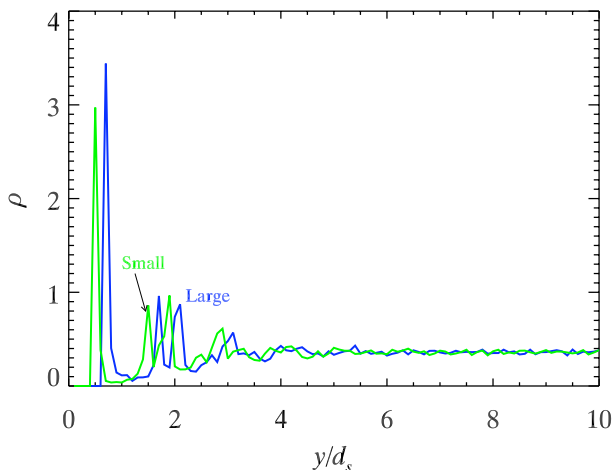


FIG. 4: A plot of the number density $\rho(y)$ for 100 2D configurations at $h = 30$ averaged together. The plot is constructed by treating the small and big particles separately and using bins along the confining direction of width $\delta y = 0.1d_s$.

curve in Fig. 3) was carried out by assuming that to first order $\phi \sim \phi_{h \rightarrow \infty} - C/h$ for large h , where $\phi_{h \rightarrow \infty} = \phi_{rcp}$ (the bulk value for the *rcp* packing) and C is a fitting parameter.

The data in Fig. 3 begin to deviate from the fit for $h \lesssim 6$, and furthermore $\phi(h)$ is not monotonic. While some of the variability is simply noise due to the finite number of disks N used in each simulation, some of the variability is real. The inset in Fig. 3 shows a magnified view of the region $3 \leq h \leq 6$. The vertical lines in this inset are located at specific values of h that can be expressed as the integer sums of the two particle diameters. For instance, the first vertical line near the y -axis is located at $h = 2d_s + d_l$. These lines are placed at some h values where $\phi(h)$ has notable spikes or plateaus. These lines suggest that there exist special values of h where the confining thickness is the right width so that particles can pack either much more efficiently or much less efficiently than nearby values of h . Intriguingly, these special h values are not the set of all possible integer sums, but instead only the selected few drawn in the figure. For example, there is no apparent feature near $h = 4$ (recall that h is nondimensionalized by d_s). Somewhat surprisingly, the peaks correspond to integer combinations of d_s and d_l , rather than combinations such as $\sqrt{3}/2d_s$. The latter would suggest hexagonal packing, the easiest packing of monodisperse disks in 2D; whereas the observed peaks of $\phi(h)$ suggest square-like packing.

To measure structural changes in particle packing as a result of confinement we start by examining the variations in the local number density ρ with distance y from the confining wall. Figure 4 is a plot of $\rho(y)$ for 100 configurations averaged together at $h = 30$. This plot shows oscillations in particle density which decay to a plateau. The oscillations near the wall are indicative of particles layering in bands. Above $y \gtrsim 6d_s$, noise masks these

oscillations. This supports our interpretation, that confinement modifies the structure near the walls but not in the interior. Furthermore, the rapidity of the decay to the plateau seen in Fig. 4 suggests that confinement is only a slight perturbation to systems with overall size $h \gtrsim 6$.

The details of the density profiles in Fig. 4 also suggest how particles pack near the wall. The small particle density (solid line) has an initial peak at $y = 0.5d_s$, indicating a large amount of small particles in contact with the wall, as their centers are one radius away from $y = 0$. Likewise, the large particle density (dashed line) has its initial peak at $y = 0.7d_s = 0.5d_l$, indicating that those particles are also in contact with the wall. This is consistent with the pictures shown in Fig. 2(a,b), where it is clear that particles pack closely against the walls. Examining again the small particle number density in Fig. 4 (solid line), the secondary peaks occur at $y = 1.5d_s$ and $y = 1.9d_s = 0.5d_s + 1.0d_l$, which is to say either one small particle diameter or one large particle diameter further away from the first density peak at $y = 0.5d_s$. This again is consistent with particles packing diameter-to-diameter, rather than “nesting” into hexagonally packed regions. Similar results are seen for the large particles (dashed line) which have secondary peaks at $y = 1.0d_s + 0.5d_l$ and $y = 2.1d_s = 1.5d_l$.

To confirm that these density profile results apply for a variety of thicknesses h , and more importantly to see how these results are modified for very small h , we use an image representation shown in Fig. 5. To create this image, density distributions of different h are each separately rescaled to a maximum value of 1. Every data point within each distribution is then made into a gray scale pixel indicating its relative value; black is a relative value of 1, and white is a relative value of 0. The vertical axis is the confining width and the horizontal axis is the distance y from the bottom wall. Each horizontal slice (constant h) is essentially the same sort of distribution shown in Fig. 4. The white space on the right side of the figure arises because the distribution is only plotted for the range $0 \leq y \leq h/2$. The distributions are symmetric about $y = h/2$, and by averaging the distribution found for the range $0 \leq y \leq h/2$ with the distribution found for the range $h/2 \leq y \leq h$, the statistics are doubled. The area shown in the box is a magnified view of that region where the full range $0 \leq y \leq h$ is being shown.

In Fig. 5 there are vertical strips of dark areas, once again indicating that particles are forming layers. The width of these strips widens and the intensity lessens farther from the wall. In each plot, the first vertical black strip is sharply defined and located at one particle radius, illustrating that small and big particles are in contact with the wall. Finally, the location and width of each layer remains essentially the same for different h , suggesting that layering arises from a constraint imposed by the closest boundary. Given that the first layer of particles always packs against the wall, this imposes a further constraint on how particles pack in the nearby vicinity.

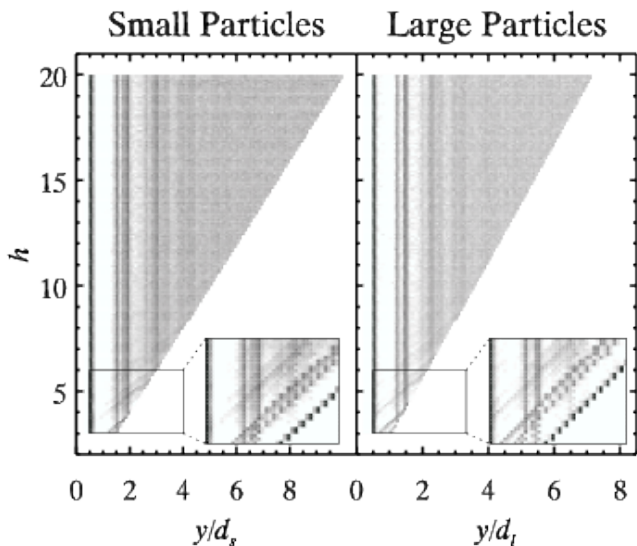


FIG. 5: An image representation constructed for the purpose of comparing 2D $\rho(y)$ distributions at many different h . The intensities have been logarithmically scaled. The vertical pixel width is 0.1 and for the left plot the horizontal pixel width is 0.2 and for the right plot the horizontal pixel width is 0.14.

The consistency in the location and width of the second layer for all h demonstrates that the constraint of the first layer always produces a similar packing in the second layer, essentially independent of h . Continuing this argument, each layer imposes a weaker constraint on the formation of a successive layer, allowing for the local packing to approach rcp far from the wall.

In the magnified views of Fig. 5, the vertical dark lines show the layering of particles induced by the left boundary and the angled dark lines show the layering of particles induced by the right boundary. We see that for small h these sets of lines overlap and intersect, meaning that there is a strong influence from one boundary on the packing within the layers produced by the other boundary. This may explain the variations seen in $\phi(h)$ for small h in Fig. 3. In particular, it is clear that at certain values of h , the layers due to one wall are coincident with the layers due to the other wall, and this suggests why $\phi(h)$ has a higher value for that particular h . Given that the layer spacings correspond to integer combinations of d_s and d_l , the coincidence of layers from both walls will correspond to integer combinations of d_s and d_l , and this thus gives insight into the peak positions shown in the inset of Fig. 3.

As described above, the influence of the walls diminishes rapidly with distance y away from the wall. In particular, for the local number density $\rho(y)$, we observe that the asymptotic limit $\rho(y \rightarrow \infty) = 0.362$ for the curves shown in Fig. 4 is in agreement with the theoretical number density of an rcp configuration $\rho_{rcp} = 4\phi_{rcp}/\pi(1+\sigma)$. To quantify the approach to the asymptotic limit, we define a length scale from a spatially varying function $f(y)$

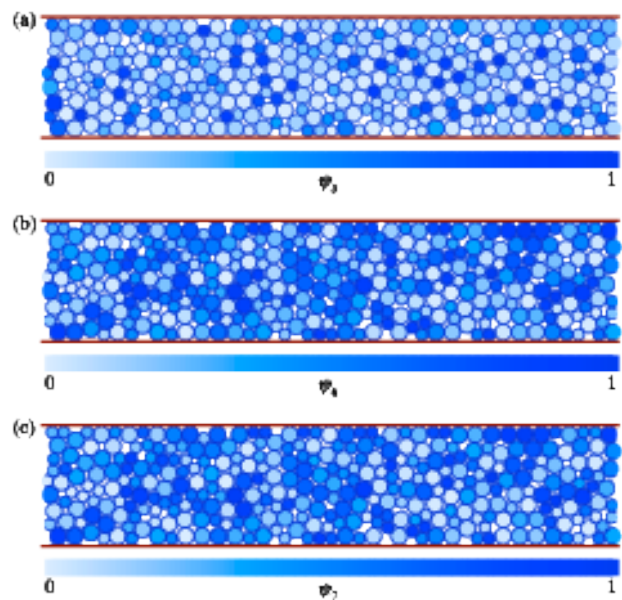


FIG. 6: (Color online). Drawings illustrating the conceptual meaning of (a) ψ_5 , (b) ψ_6 , and (c) ψ_7 . Darker colored particles have neighbors that are packed more like an ideal regular n -sided polygon as compared to lighter drawn particles. The configuration of particles is the same for all panels, and are drawn from a simulation with $h = 10$. Note in (b) that there are no large patches of high ψ_6 , demonstrating that there are no large crystalline domains.

using:

$$\lambda = \frac{\int y [f(y) - f(y \rightarrow \infty)]^2 dy}{\int [f(y) - f(y \rightarrow \infty)]^2 dy}. \quad (2)$$

In this equation $f(y)$ is an arbitrary function where the value of λ quantifies the weighting of $f(y)$. For simple exponential decay $f(y) = Ae^{(-y/\lambda')}$, Eqn. 2 gives $\lambda = \lambda'/2$. Using $f(y) = \rho(y)$ we find $\lambda = 0.85d_s$ and $\lambda = 0.72d_s$ for the small particle curve and big particle curve in Fig. 4 respectively, suggesting that the transition from wall-influenced behavior to bulk rcp packing happens extremely rapidly.

To further investigate the convergence of the local packing to rcp more closely we analyze the local bond order parameters ψ_n , which for a disk with center of mass r_i are defined as

$$\psi_n(r_i) = \frac{1}{n_b} \sum_j e^{ni\theta(r_{ij})}. \quad (3)$$

The sum is taken over all j particles that are neighbors of the i th particle, $\theta(r_{ij})$ is the angle between the bond connecting particles i and j and an arbitrary fixed reference axis, and n_b is the total number of $i-j$ bonds [63]. The magnitude of ψ_n is bounded between zero and one; the closer the magnitude of ψ_n is to 1, the closer the local arrangement of neighboring particles are to an ideal

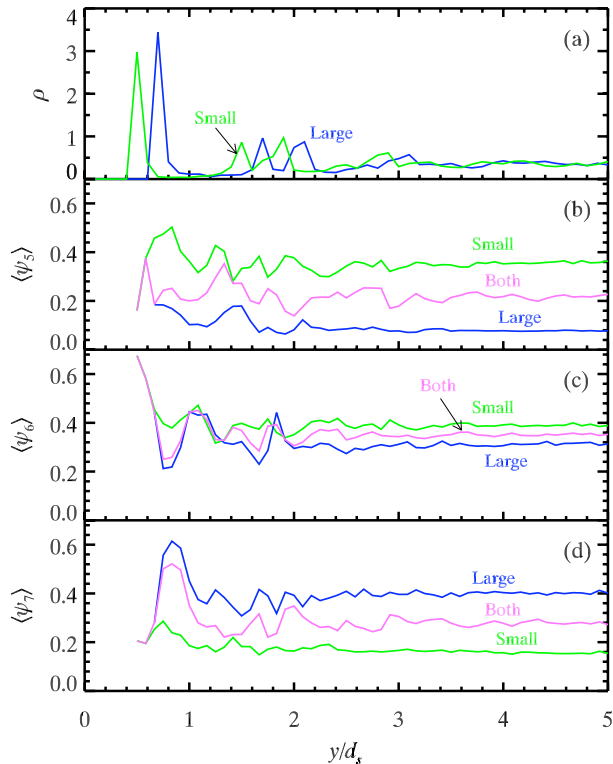


FIG. 7: (Color online). (a) is a plot of the local number density $\rho(y)$ for 2D configurations of big and small particles separately. (b) - (d) are plots of $\langle\psi_n\rangle(y)$ for small (green/light gray) and big particles (blue/dark gray) separately, and both sizes together (light purple/medium gray) where (b) is $\langle\psi_5\rangle$, (c) is $\langle\psi_6\rangle$, and (d) is $\langle\psi_7\rangle$. The length scales determined from these curves for small, large, and both species are $\lambda_{5,s} = 1.2$, $\lambda_{5,l} = 1.1$, $\lambda_{5,b} = 1.4$, $\lambda_{6,s} = 0.8$, $\lambda_{6,l} = 0.9$, $\lambda_{6,b} = 0.8$, $\lambda_{7,s} = 1.1$, $\lambda_{7,l} = 0.7$, and $\lambda_{7,b} = 1.0$ (all in terms of d_s).

n -sided polygon. Figures 6(a-c) are drawings illustrating the concept of ψ_n using a 2D configuration with $h = 10$. Particles with larger ψ_n are drawn darker. These figures have no large clusters of dark colored particles, demonstrating that there are no large crystalline domains (i.e. particles are randomly packed).

For a highly ordered monodisperse packing $\langle\psi_6\rangle$ would be the most appropriate choice for measuring order because of the ability for monodisperse packings to form hexagonal packing. However for a bidisperse packing with size ratio $\sigma = 1.4$, the average number of neighbors a small particle will have is 5.5 and the average number of neighbors big particles will have is 6.5. Therefore, a bidisperse packing of this kind will have a propensity to form local pentagonal, hexagonal, and heptagonal packing, and to properly investigate how the local packing varies we examine $\langle\psi_5\rangle$, $\langle\psi_6\rangle$, and $\langle\psi_7\rangle$. We compute the average values $\langle\psi_5\rangle$, $\langle\psi_6\rangle$, and $\langle\psi_7\rangle$ for all configurations as a function of y , and averaging together all $\langle\psi_n\rangle$ distributions for configurations with $h \geq 16$ to improve

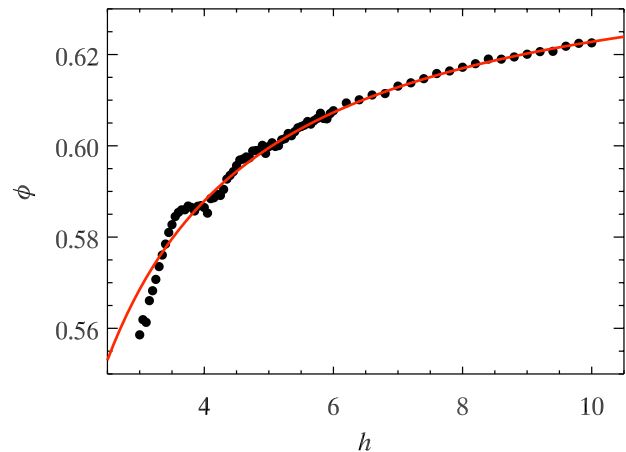


FIG. 8: The black data points are the average packing fractions of 3D configurations at various h . The red (dark gray) curve is a fit from our model Eqn. 5. For each h at least 10 configurations were averaged together.

statistics. This averaging can be justified by considering that oscillations in $\rho(y)$ in Fig. 4 for $y/d_s > 10$ are quite small. Thus this averaging improves our statistics for the range $0 < y/d_s < 5$ where the largest oscillations occur, without skewing the data. In the end nearly 10,000 configurations are averaged together, producing the curves shown in Fig. 7(b-d). This figure shows the spatial variations of $\langle\psi_5\rangle$, $\langle\psi_6\rangle$, and $\langle\psi_7\rangle$ for small and big particles separately and both particles combined. All curves show fluctuations that decay with distance from the wall, and show local order within and between layers. Figure 7(a) has been added so comparisons between the location of the oscillations in $\rho(y)$ and $\langle\psi_n\rangle(y)$ can be made.

For the most part, each successive layer has less orientational order than the previous layer with $\langle\psi_n\rangle$ eventually decaying to an asymptotic limit. To characterize a length scale for these curves we compute λ using Eqn. 2 for each curve shown in Fig 7(b-d). From the nine curves, we find that the mean value of $\lambda = (1.00 \pm 0.24)d_s$. The length scales found for these curves are once again less than the largest particle diameter. No striking difference is found between the different order parameters or between the different particle sizes; specific values of λ are given in the figure caption. (Note that the asymptotic limits of all $\langle\psi_n\rangle$ plots are in agreement with the average values found for 40 unconfined 10,000 particle simulations averaged together, confirming that the local packing converges to an *rcp* arrangement far from the walls.)

Next, we wish to distinguish the structural influence of the flat wall from the finite size effects. We perform simulations where the confining wall is replaced by a periodic boundary with periodicity h ; thus particles cannot form layers. In this case, the packing fraction still decreases as h is decreased, as shown by the green curve (light gray) in Fig. 3, although the effect is less striking than for the case with walls (black curve). A likely explanation

for the decrease in ϕ with confinement is the long range structural correlations imposed along the constricted direction; in other words, if there is a particle located at (x, y) that particle is mirrored at $(x, y - h)$ and $(x, y + h)$ by the periodic boundary. We know from the pair correlation function [12, 14] of *rcp* configurations that structural correlations exist over distances of many particle diameters, although of course these are weak at larger distances. Thus the periodicity forces a deviation from the ideal *rcp* packing, that becomes more significant as h decreases. By definition *rcp* is the most random densely packed state, and thus any perturbations away from this state must have a lower packing fractions. However, this is not nearly as significant as the constraint imposed by the flat wall, as is clear comparing the green (light gray) data and the black data in Fig. 3.

B. 3D Systems

We next consider 3D confined systems. We start by investigating $\phi(h)$, shown as the black points in Fig. 8. As observed in the 2D case, ϕ is reduced as a result of confinement. However, unlike the 2D system, there does not appear to be a series of “special values” of h that give rise to peaks and plateaus, other than a hump near $h = 3.75$. The lack of substructure may be due to the smaller size in x and z , in contrast with the 2D simulations which had large sizes in the unconfined direction.

Next we investigate the local number density $\rho(y)$ for $h = 25$, shown in Fig. 9(a). The data are constructed by averaging together 100 configurations. The curve shows fluctuations that decay with distance from the wall, eventually reaching a plateau. Using Eqn. 2, we obtain decay lengths $\lambda_{3D} = 0.77d_s$ and $0.73d_s$ for the small and large particle curves respectively. These length scales are similar to the length scales obtained in the 2D case ($\lambda_{2D} = 0.85d_s$ and $0.72d_s$ for small and large particles).

To compare all 3D $\rho(y)$ distributions for different h we construct the image representation used to compare 2D configurations in Fig. 5. The data for the 3D configurations are shown in Fig. 10. Again there are dark vertical strips arising from particles forming layers near the wall. Like in 2D, the density approaches the “bulk” *rcp* value far from the wall.

In 2D, we also noted that the structure is modified near the wall, as measured by the ψ_n order parameters. To investigate structural ordering in 3D, we use a local structural parameter sensitive to ordering [64, 65]. We start by defining

$$\hat{q}_{i,6} = \frac{1}{n_j K} \sum_j Y_{6m}(\theta_{ij}, \phi_{ij}). \quad (4)$$

In the above equation $m = \{-6, \dots, 0, \dots, 6\}$, and thus $\hat{q}_{i,6}$ is a 13 element complex vector which is assigned to every particle i in the system. The sum in Eqn. 4 is taken over the j nearest neighbors of the i th particle, n_j is the total

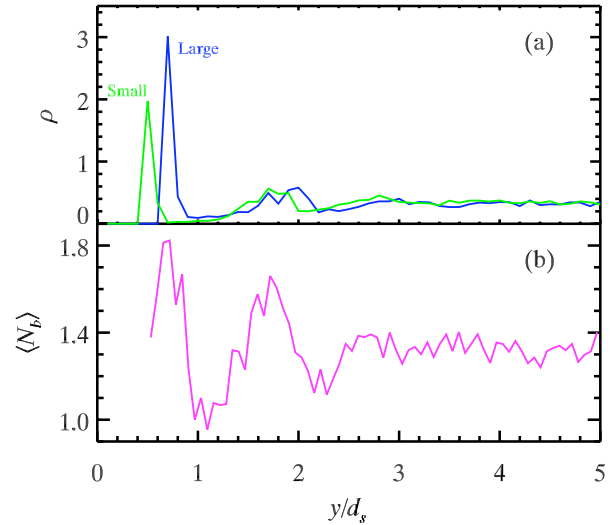


FIG. 9: (a) is plot of $\rho(y)$ for 3D configurations for small and big particles separately. The plot is constructed using bins of width $\delta y = 0.1d_s$ along the confining directions. (b) is a plot of the average number of ordered bonds $\langle N_b \rangle(y)$.

number of neighbors, and K is a normalization constant so that $\hat{q}_{i,6} \cdot \hat{q}_{i,6} = 1$. For two particles i and j that are nearest neighbors, $Y_{6m}(\theta_{ij}, \phi_{ij})$ is the spherical harmonic associated with the vector pointing from particle i to particle j , using the angles θ_{ij} and ϕ_{ij} of this vector relative to a fixed axis. Next, any two particles m and n are considered “ordered neighbors” if $\hat{q}_{m,6} \cdot \hat{q}_{n,6} > 0.5$ [64, 65]. Finally, we quantify the local order within the system by the number of ordered neighbors N_b a particle has.

Figure 9(b) is a plot of the average number of ordered neighbors particles have $\langle N_b \rangle$ as a function of distance y from the wall. In comparison with Fig. 9(a), this plot shows that local order is mostly seen within layers, not between layers. Also we see that $\langle N_b \rangle$ converges to an asymptotic value of ≈ 1.3 , confirming that the system is disordered (values of $N_b > 8$ are considered crystalline [65]). We use Eqn. 2 to characterize a length scale for the decay in $\langle N_b \rangle$, giving $\lambda = 1.3d_s$. The asymptotic limit of $\langle N_b \rangle(y)$ in Fig. 9(b) agrees with the average value of N_b found for 15 large simulations with 2,500 particles and periodic boundary conditions, confirming that the local structure in the confined case converges to the bulk *rcp* state far from the walls.

Our results show that in both 2D and 3D, confinement induces changes in structural quantities near the walls, with a decay towards the “bulk” values characterized by length scales no larger than d_i . The only prior work we are aware of with related results are a computational study [46] and an experimental study [47] of collections of monodisperse particles confined in a large silo. The simulation by Landry et al. primarily focused on the force network within the silo. They show one plot of the local

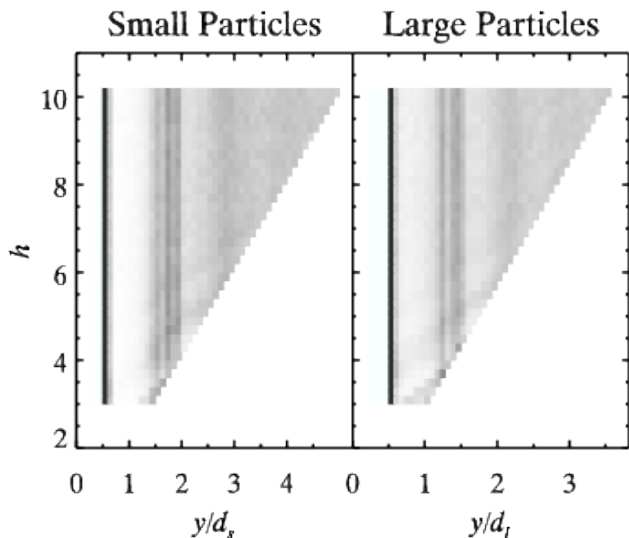


FIG. 10: An image representation comparing the number density distributions of 3D configurations for many different h . Black pixels represents a relative value of 1 and white represent a relative value of 0. A gray scale is used to represent relative values between 0 and 1. The pixel widths are $0.1d_s$ horizontally and 0.2 vertically.

packing fraction as a function of distance from the silo wall. Similar to our results, this local packing fraction showed fluctuations that decayed monotonically. In their paper they state a decay length of $\approx 4d_l$; however, it appears that they drew this conclusion by estimating the value by eye. Applying Eqn. 2 to their data we find λ on the order of d_l , close to the value found in our simulations. The experimental study by Seidler et al. reported on the local bond orientational order parameter which showed oscillation that decayed with distance from the wall. They reported a decay length of $\lambda \approx d_l$ using an exponential fit. The length scales from these two studies are slightly larger than those found in our work.

IV. MODEL

Our results for $\phi(h)$ can be understood with a simple model incorporating an effective boundary layer and a bulk like region. Figure 11 shows a configuration of particles confined between two plates and divided into three regions. Near each confining wall particles show strong layering and will assume a configuration much different than rcp . For this model, these particles will be replaced by an effective “boundary layer” with packing fraction ϕ_l . Layering will persist far into the bulk, but after some distance, indicated in the figure by δL , the local packing of particles will be near that of rcp . Particles in the bulk region will be approximated to be in a rcp configuration with packing fraction ϕ_{rcp} . Using this simple model, ϕ can be approximated by the weighted average $\phi = \frac{h-2\delta L}{h}\phi_{rcp} + \frac{2\delta L}{h}\phi_l$ (in either 2D or 3D, with of course

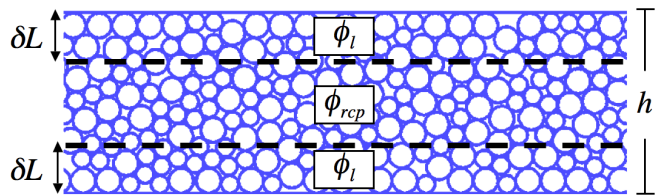


FIG. 11: (Color online). Illustration of our model for $\phi(h)$. Our model breaks a configuration with confining width h into three regions. The boundary layers are approximated to have a packing fraction ϕ_l and persist a distance δL into the sample, and the middle “bulk” region is approximated to have a packing fraction ϕ_{rcp} .

different values of the parameters depending on the dimension.) Reducing this equation further we obtain

$$\phi = \phi_{rcp} - \frac{C}{h}, \quad (5)$$

where $C = 2\delta L(\phi_{rcp} - \phi_l)$. Note that this is the same form for $\phi(h)$ obtained from considering a 1st order correction in terms of $1/h$.

Equation 5 only contains two fitting parameters, ϕ_{rcp} and C . ϕ_{rcp} is the packing fraction of an infinite unconfined configuration, and C approximates the difference in ϕ from ϕ_{rcp} for the first layers contained within a distance δL from the confining wall. The data in both Fig. 3 and Fig. 8 are fitted to Eqn. 5. The fits are shown as the red lines (dark gray) in the earlier figures, and also in Fig. 12, where the data are plotted as functions of $1/h$ to better illustrate the success of this model. The fits give for 2D $\phi_{rcp} = 0.844$ and $C = 0.317$ and for 3D $\phi_{rcp} = 0.646$ and $C = 0.233$. Both fits give values for ϕ_{rcp} that are slightly larger, but not by much, than ϕ_{rcp} reported earlier in the paper. In Fig. 12 it can be seen that the packing fraction for large $1/h$ dip significantly below the fitting line, due to the fluctuations in $\phi(h)$ for small h ; this is responsible for the over estimate in ϕ_{rcp} . When the data for both curves are fitted for $h \geq 8$ ($1/h < 0.125$) the actual values for ϕ_{rcp} are obtained.

To provide further credence to our model we also perform 2D rcp simulations with a fixed circular boundary. Our simulations were carried out with different confining widths ranging from $h \approx 10 - 40$, where h is the diameter of the circular boundary normalized by d_s . Figure 13 shows a plot of $\phi(h)$ for a circular fixed boundary. As before with a flat boundary condition, we see that ϕ increases to an asymptotic limit. Adapting our model to a curved boundary with radius $R = h/2$, the weighted average becomes $\phi(R) = \frac{\pi[R^2 - (R - \delta L)^2]}{\pi R^2}\phi_{rcp} + \frac{\pi(R - \delta L)^2}{\pi R^2}\phi_l$. This expression can be simplified as $\phi = \phi_{rcp} - 2C/h$, using $C = 2\delta L(\phi_{rcp} - \phi_l)$ as before, and dropping a term that is second order in $\delta L/h$. We show this curve as the red line (light gray) curve in Fig. 13, using the same values from our prior 2D fit with non-curved walls ($\phi_{rcp} = 0.844$, $C = 0.317$), and find good agreement with the data. A direct fit to the circular data gives

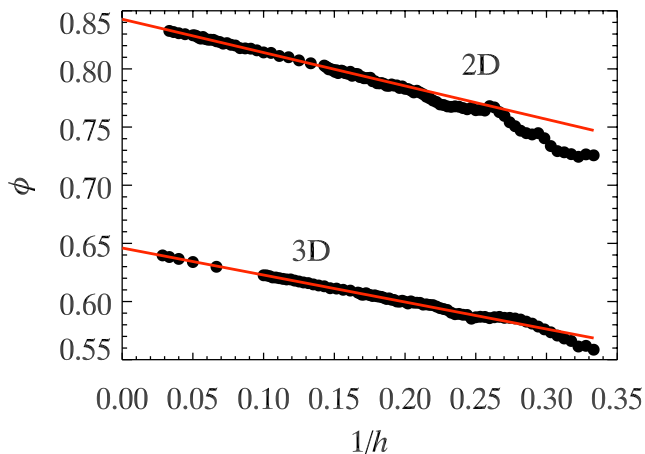


FIG. 12: (Color online). The upper black curve is a plot of $\phi(1/h)$ for 2D configurations, and the red (dark gray) line going through the curve, is a fit from our model. Likewise, the lower black curve is a plot of $\phi(1/h)$ for 3D configurations with the red (dark gray) line going through the curve being another fit from our model.

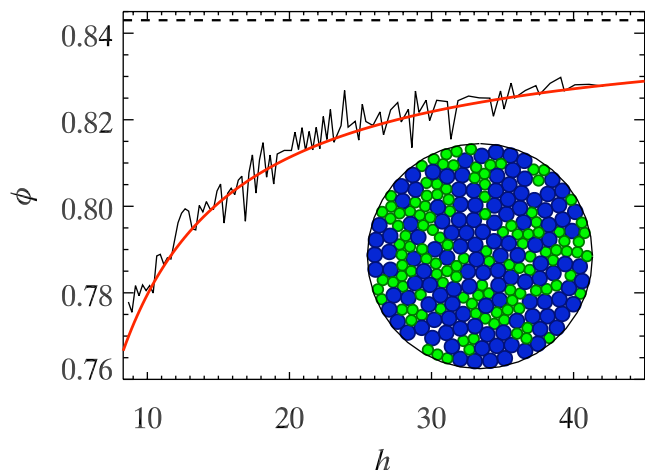


FIG. 13: (Color online). The black curve is the packing fraction dependence of random close packed 2D disks enclosed within a circular boundary. The red (light gray) curve is from our model using the parameters appropriate to Fig. 12 (2D case). The image at the lower right is an rcp configuration confined in a circular boundary with $h = 21$. Small particles are rendered as green (medium gray) and large particles are rendered as blue (dark gray).

$\phi_{rcp} = 0.843$ and $C = 0.301$; the slightly smaller value of C suggests that particles pack more efficiently near a curved boundary than a flat boundary. However, within the uncertainty of our limited data in the curved geometry, it is not clear if the difference in C is significant.

V. CONCLUSION

In this paper, we have shown how a confining boundary alters the structure of random close packing by investi-

gating simulated *rcp* configurations confined between two walls in 2D and 3D. We find that confinement lowers the packing fraction, and induces heterogeneity in particle density where particles layer in bands near the wall. The structure of the local packing decays from a more ordered packing near the wall to a less ordered packing in the bulk. All measures of local order and local density decay rapidly to their bulk values with characteristic length scales on the order of particle diameters. Thus, the influence of the walls is rapidly forgotten in the interior of the sample, with confinement having the most notable effects when the confining dimension is quite small, perhaps less than 10 particle diameters across.

These findings have implications for experiments investigating the dynamics of densely packed confined systems (i.e. colloidal suspensions or granular materials). For example, our work shows that for small h the packing fraction has significant variations at small h (mostly clearly seen in 2D, for example Fig. 3). For dense particulate suspensions with $\phi < \phi_{rcp}$, flow is already difficult. By choosing a value of h with a local maximum in $\phi_{rcp}(h)$, a suspension may be better able to flow, as there will be more free volume available. Likewise, a poor choice of h may lead to poor packing and enhanced clogging. A microfluidic system with a tunable size h may be able to vary the flow properties significantly with small changes of h , but our work implies that control over h needs to be fairly careful to observe these effects. Of course, these effects will be obscured by polydispersity in many systems of practical interest; however, our work certainly has implications for microfluidic flows of these sorts of materials, once the minimum length scales approach the mean particle size.

Our work has additional implications for experiments on confined glasses [28, 50, 51, 52, 53, 54, 55, 56, 57]. As mentioned in the introduction, confinement changes the properties of glassy samples, but it is unclear if this is due to finite size effects or due to interfacial influences from the confining boundaries [58]. Our results show that dense packings have significant structural changes near the flat walls, suggesting that indeed interfacial influences on materials can be quite strong at very short distances, assuming that the structural changes couple with dynamical behavior.

Acknowledgments

This work was supported by the National Science Foundation under Grant No. DMR-0804174.

-
- [1] F. Zamponi, *Nature* **453**, 606 (2008).
 - [2] J. C. Hales, *Ann. Math.* **162**, 1065 (2005).
 - [3] G. D. Scott and D. M. Kilgour, *J. Phys. D Appl. Phys.* **2**, 863 (1969).
 - [4] J. G. Berryman, *Phys. Rev. A* **27**, 1053 (1983).
 - [5] G. Y. Onoda and E. G. Liniger, *Phys. Rev. Lett.* **64**, 2727 (1990).
 - [6] J. D. Bernal and J. Mason, *Nature* **188**, 910 (1960).
 - [7] C. S. O'Hern, S. A. Langer, A. J. Liu, and S. R. Nagel, *Phys. Rev. Lett.* **88**, 075507 (2002).
 - [8] N. Xu, J. Blawdziewicz, and C. S. O'Hern, *Phys Rev E* **71**, 061306 (2005).
 - [9] S. Torquato, T. M. Truskett, and P. G. Debenedetti, *Phys. Rev. Lett.* **84**, 2064 (2000).
 - [10] W. S. Jodrey and E. M. Tory, *Phys. Rev. A* **32**, 2347 (1985).
 - [11] J. Tobochnik and P. M. Chapin, *J. Chem. Phys.* **88**, 5824 (1988).
 - [12] A. R. Kansal, S. Torquato, and F. H. Stillinger, *J. Chem. Phys.* **117**, 8212 (2002).
 - [13] R. Al-Raoush and M. Alsaleh, *Powder Technol.* **176**, 47 (2007).
 - [14] K. Lochmann, L. Oger, and D. Stoyan, *Solid State Sci.* **8**, 1397 (2006).
 - [15] P. Richard, L. Oger, J. P. Troadec, and A. Gervois, *Eur. Phys. J. E* **6**, 295 (2001).
 - [16] H. J. H. Brouwers, *Phys. Rev. E* **74**, 031309 (2006).
 - [17] A. Donev, I. Cisse, D. Sachs, E. A. Variano, F. H. Stillinger, R. Connelly, S. Torquato, and P. M. Chaikin, *Science* **303**, 990 (2004).
 - [18] T. Okubo and T. Odagaki, *J Phys.-Condens. Mat.* **16**, 6651 (2004).
 - [19] K. Desmond and S. V. Franklin, *Phys. Rev. E* **73**, 031306 (2006).
 - [20] Y. Jiao, F. H. Stillinger, and S. Torquato, *Phys. Rev. Lett.* **100**, 245504 (2008).
 - [21] S. F. Edwards, *Granular Matter* (Springer-Verlag, 1994).
 - [22] C. Radin, *J. Stat. Phys.* **131**, 567 (2008).
 - [23] P. Jalali and M. Li, *J. Chem. Phys.* **120**, 1138 (2004).
 - [24] C. Song, P. Wang, and H. A. Makse, *Nature* **453**, 629 (2008).
 - [25] R. Pal, *Polym. Eng. Sci.* **48**, 1250 (2008).
 - [26] G. Lois, J. Blawdziewicz, and C. S. O'Hern, *arXiv:0809.1044* (2008).
 - [27] R. Zallen, *Physics of Amorphous Solids* (Wiley, 1983).
 - [28] M. Alcoutlabi and G. B. McKenna, *J Phys.-Condens. Mat.* **17**, R461 (2005).
 - [29] P. Gallo, M. Rovere, and E. Spohr, *J. Chem. Phys.* **113**, 11324 (2000).
 - [30] S. Granick, *Science* **253**, 1374 (1991).
 - [31] J. R. Henderson, *Mol. Phys.* pp. 2345–2352 (2007).
 - [32] J. Mittal, V. K. Shen, J. R. Errington, and T. M. Truskett, *J. Chem. Phys.* **127**, 154513 (2007).
 - [33] J. Mittal, J. R. Errington, and T. M. Truskett, *J. Chem. Phys.* **126**, 244708 (2007).
 - [34] J. Mittal, T. M. Truskett, J. R. Errington, and G. Hummer, *Phys. Rev. Lett.* **100**, 145901 (2008).
 - [35] I. Cohen, T. G. Mason, and D. A. Weitz, *Phys. Rev. Lett.* **93**, 046001 (2004).
 - [36] K. To, P.-Y. Lai, and H. K. Pak, *Physica A* **315**, 174 (2002).
 - [37] I. Zuriguel, L. A. Pugnaloni, A. Garcimartín, and D. Maza, *Phys. Rev. E* **68**, 030301 (2003).
 - [38] S. Redner and S. Datta, *Phys. Rev. Lett.* **84**, 6018 (2000).
 - [39] S. B. Fuller, E. J. Wilhelm, and J. M. Jacobson, *J. Microelectromech S.* **11**, 54 (2002).
 - [40] K. Sharp and R. Adrian, *Microfluid Nanofluid* **1**, 376 (2005).
 - [41] G. M. Whitesides, *Nature* **442**, 368 (2006).
 - [42] L. Vanel, P. Claudin, Bouchaud, M. E. Cates, E. Clément, and J. P. Wittmer, *Phys. Rev. Lett.* **84**, 1439 (2000).
 - [43] U. Marconi, *Physica A* **280**, 279 (2000).
 - [44] P. Claudin and J.-P. Bouchaud, *Phys. Rev. Lett.* **78**, 231 (1997).
 - [45] J. W. Landry, G. S. Grest, and J. Plimpton, *Powder Technol.* **139**, 223 (2004).
 - [46] J. W. Landry, G. S. Grest, L. E. Silbert, and S. J. Plimpton, *Phys. Rev. E* **67**, 041303 (2003).
 - [47] G. T. Seidler, G. Martinez, L. H. Seeley, K. H. Kim, E. A. Behne, S. Zaraneek, B. D. Chapman, S. M. Heald, and D. L. Brewe, *Phys. Rev. E* **62**, 8175 (2000).
 - [48] L.-W. Teng, P.-S. Tu, and I. Lin, *Phys. Rev. Lett.* **90**, 245004 (2003).
 - [49] C. Murray, *MRS Bulletin* **23**, 33 (1998).
 - [50] Z. T. Németh and H. Löwen, *Phys. Rev. E* **59**, 6824 (1999).
 - [51] C. R. Nugent, K. V. Edmond, H. N. Patel, and E. R. Weeks, *Phys. Rev. Lett.* **99**, 025702 (2007).
 - [52] D. Morineau, Y. Xia, and C. A. Simionescu, *J. Chem. Phys.* **117**, 8966 (2002).
 - [53] J. Schüller, Y. Mel'nichenko, R. Richert, and E. W. Fischer, *Phys. Rev. Lett.* **73**, 2224 (1994).
 - [54] C. L. Jackson and G. B. McKenna, *J. Non-Cryst. Solids.* **131-133**, 221 (1991).
 - [55] K. Kim and R. Yamamoto, *Phys. Rev. E* **61**, R41 (2000).
 - [56] P. A. Thompson, G. S. Grest, and M. O. Robbins, *Phys. Rev. Lett.* **68**, 3448 (1992).
 - [57] P. Scheidler, W. Kob, K. Binder, and G. Parisi, *Philos. Mag. A* **82**, 283 (2002).
 - [58] F. He, L. M. Wang, and R. Richert, *Eur. Phys. J. Special Topics* **141**, 3 (2007).
 - [59] A. S. Clarke and J. D. Wiley, *Phys. Rev. B* **35**, 7350 (1987).
 - [60] J. Nocedal and S. J. Wright, *Numerical Optimization* (Springer, 1999).
 - [61] A. Donev, S. Torquato, F. H. Stillinger, and R. Connelly, *Phys. Rev. E* **70**, 043301 (2004).
 - [62] C. S. O'Hern, L. E. Silbert, A. J. Liu, and S. R. Nagel, *Phys. Rev. E* **70**, 043302 (2004).
 - [63] A. H. Marcus and S. A. Rice, *Phys. Rev. Lett.* **77**, 2577 (1996).
 - [64] P. J. Steinhardt, D. R. Nelson, and M. Ronchetti, *Phys. Rev. B* **28**, 784 (1983).
 - [65] U. Gasser, E. R. Weeks, A. Schofield, P. N. Pusey, and D. A. Weitz, *Science* **292**, 258 (2001).